

Autophagy is induced during plant grafting to promote wound healing

Received: 27 December 2023

Accepted: 21 March 2025

Published online: 12 April 2025

 Check for updates

Ken-ichi Kurotani^{1,10}, Daiki Shinozaki^{2,3,10}, Kentaro Okada^{1,10}, Ryo Tabata^{4,10}, Yaichi Kawakatsu^{1,10}, Ryohei Sugita^{5,6}, Yuki Utsugi², Koji Okayasu⁴, Moe Mori⁴, Keitaro Tanoi⁵, Yumi Goto⁷, Mayuko Sato⁷, Kiminori Toyooka⁷, Kohki Yoshimoto²✉ & Michitaka Notaguchi^{1,4,8,9}✉

Grafting is an agricultural technique that joins tissues from different plants to obtain useful rootstock traits. However, cellular processes involved in joint tissue repair remain poorly understood. We analyzed *Nicotiana benthamiana* (*Nb*) and *Arabidopsis thaliana* (*At*) interfamily heterografting as a high-stress model and *At* homografting as a low-stress model. Transmission electron micrographs reveal the formation of autophagic structures in cells near the graft boundary over a long period in *Nb/At* interfamily grafts and in a short period of a few days in *At* homografts. Using a GFP-ATG8 marker line, the autophagosomes were observed in the cells near the graft boundary, especially on the scion side, where nutrient depletion occurred. Grafting of *At* autophagy-defective mutants decreases grafting success rates and post-grafting growth. *NbATG5* knockdown suppresses graft establishment in *Nb/At* interfamily heterografts. Moreover, *At* autophagy-defective mutants show reduced callus formation directed to wounds under the nutrient-deficient conditions. These results suggest that autophagy is induced during grafting, promoting callus formation and contributing to tissue connectivity.

Grafting is an important method in agriculture to propagate heterogeneous but attractive ornamental and fruit tree species and/or to benefit from rootstock traits, such as disease resistance and tolerance to unfavorable soils, in the cultivation of fruit and vegetable crops¹. Grafting can lead to phenotypic variation through the molecular transport of RNA, DNA, and protein^{2,3}. The potential utility of grafting has recently been expanded to include a broad range of interfamilial combinations^{4–6} and intra- and inter-monocotyledonous species⁷ in combination with time-course information on the transcriptomic dynamics of grafted tissues. The process of graft formation has been

described at the morphological and molecular levels in various plant species, including grape^{8,9}, litchi¹⁰, tomato^{11,12}, cucurbit¹³, and the model plant *Arabidopsis thaliana* (*At*)^{14–16}. Structural studies on grafting processes demonstrated that grafting is achieved through a sequential wound response, callus bridge formation, adhesion, differentiation of wound-repairing vascular tissues, and production of secondary xylem and phloem in the callus bridge¹. Ultrastructural analyzes of the graft boundary region showed that one or two necrotic layers of damaged cells initially lay between the rootstock and scion and the layer was fragmented 2–3 days after grafting (DAG) as callus

¹Bioscience and Biotechnology Center, Nagoya University, Nagoya, Japan. ²Department of Life Sciences, School of Agriculture, Meiji University, Kawasaki, Japan. ³Organization for the Strategic Coordination of Research and Intellectual Properties, Meiji University, Kawasaki, Japan. ⁴Graduate School of Bioagricultural Sciences, Nagoya University, Nagoya, Japan. ⁵Isotope Facility for Agricultural Education and Research, Graduate School of Agricultural and Life Sciences, The University of Tokyo, Tokyo, Japan. ⁶Radioisotope Research Center, Nagoya University, Nagoya, Japan. ⁷Center for Sustainable Resource Science, RIKEN, Yokohama, Japan. ⁸Department of Botany, Graduate School of Science, Kyoto University, Kyoto, Japan. ⁹National Key Laboratory for Germplasm Innovation and Utilization for Fruit and Vegetable Horticultural Crops, College of Horticulture and Forestry Sciences, Huazhong Agricultural University, Wuhan, Hubei Province, China. ¹⁰These authors contributed equally: Ken-ichi Kurotani, Daiki Shinozaki, Kentaro Okada, Ryo Tabata, Yaichi Kawakatsu. ✉e-mail: kohki_yoshimoto@meiji.ac.jp; notaguchi.michitaka.4k@kyoto-u.ac.jp

proliferation continued¹⁷. Newly proliferated calli from peripheral tissues produce a fibrillary network and bead-like structures on the cell surface and the extracellular material subsequently seals the graft union^{18,19}. Plasmodesmata are newly formed in the cell wall region at the graft boundary, especially where vascular tissues are well aligned between the rootstock and scion^{20–22}. Thus, a sequence of cell adhesion processes has been described during wound healing.

In eukaryotic cells, autophagy is a universal mechanism for discarding damaged or harmful components and recycling cellular materials during development^{23–25}. The function of autophagy has been speculated based on ultrastructural observations using electron microscopy. In cells in which autophagy is activated, the bulk sequestration of cytoplasmic fragments and subsequent digestion in lytic vacuoles are observed. Three distinct types of autophagy have been reported in plants: macroautophagy, microautophagy, and mega-autophagy^{26,27}. The molecular mechanisms underlying autophagy are best understood in terms of macroautophagy. Macroautophagy is a major pathway involved in the transport of intracellular components via membrane dynamics. A lipid bilayer, called an isolation membrane, forms in the cytoplasm and envelopes the cytoplasm and organelles to form bilayer vesicles called autophagosomes. Autophagosomes fuse with the membranes of vacuoles and lysosomes, releasing the inner membrane structure of autophagic bodies. Autophagic bodies then degrade the target material together with the inner membrane of the autophagosome via hydrolytic enzymes in the vacuole or lysosome. Macroautophagy depends on approximately 40 core *AUTOPHAGY-RELATED* (*ATG*) genes that are highly conserved from yeasts to mammals and plants. In plants, the transcript levels of many *ATG* genes increase during senescence and nutritional starvation. Among the encoded proteins, ATG3, ATG4, ATG5, ATG7, ATG8, ATG10, ATG12, and ATG16 constitute the two ubiquitin-like conjugation systems essential for autophagosome formation^{28,29}. ATG8 forms a conjugate with phosphatidylethanolamine to bind autophagic membranes. The abundance of this conjugate is often used as an indicator of autophagic activity, while GFP-tagged ATG8 is used to monitor autophagic structures²⁸. ATG2 forms a complex with ATG9 and ATG18 and plays an important role in lipid transport from the endoplasmic reticulum to the isolation membrane in yeast *Saccharomyces cerevisiae*^{30,31}. In *At*, autophagy is induced by carbon and nitrogen deprivation. The conjugation of ATG8/ATG12 with other ATG proteins via ATG7 is important for growth under nitrogen-deficient conditions, and the binding of ATG12 and ATG5 is essential for nutrient recycling^{32,33}. Failed autophagy activation in *atg* mutants results in a short lifespan because of early senescence and reduced fitness to environmental light conditions²⁶. Therefore, autophagy is important for plant growth and development.

This study aimed to investigate intracellular events during grafting using transmission electron microscopy. Since the autophagic structures were present at the graft boundaries of *Nicotiana benthamiana* (*Nb*)/*At* interfamily hetero-grafts a long time after grafting and *At* micrografts during graft healing, we investigated the role of autophagy for graft healing in *Nb/At* hetero- and *At* homo-graft combinations. Grafting experiments using the *At* autophagy mutants, *atg2* and *atg5*, and virus-induced gene knockdown of *NbATG5* were conducted and examined the effect of these gene knock-out and knock-down on graft establishment.

Results

Autophagic structures were observed at the graft boundary

In our previous report, we have shown that *Nb* can establish grafting even at large genetic distances of the combination, and identified factors involved in cellular adhesion at the graft boundary and subsequent rejoining of the vascular tissue through transcriptome analysis of interfamily grafts^{4,34}. To gain insight into the cellular events involved in graft healing, we analyzed the graft junction of *Nb/At* interfamily

heterografts, which endured more severe stress after grafting than practical homografts. Transverse sections of the graft junctions of the interfamily heterografts of *Nb* mature stems as scions on *At* inflorescence stems as rootstocks, as shown by the illustration in Fig. 1a, were observed at 14 DAG using an optical microscope and a transmission electron microscope (TEM) (Fig. 1 and Supplementary Fig. 1). At this stage in *Nicotiana* interfamily stem-grafting, the tissue reunion processes still progress, while in conventional homo- or intrafamily grafting of herbaceous plants, the corresponding process of which is often accomplished earlier. As previously reported, the grafting boundary between *Nb* and *At* was determined based on the differences in the shape of the plastids in the cells of each plant species⁴. Callus cells were formed at the boundary of the cambial region (Supplementary Figs. 1a, b). Numerous granular structures were observed in the vacuolar lumens of *Nb* cells near the graft boundary (Fig. 1b, c and Supplementary Fig. 1a, b). These structures appeared to be typical autophagic bodies. Such structures were not present in the cells of the intact stem tissue (Fig. 1d).

GFP-ATG8 autophagy marker was observed in the hetero-grafted tissues

We used an autophagosome marker, GFP-ATG8³⁵, expressed under the control of the actin promoter in *Nb* and *CaMV* 35S promoter in *At* to monitor autophagy activation in *Nb/At* interfamily stem-grafts. *ATG8* genes are expressed ubiquitously in cells and localized in the autophagosome when autophagy is activated, resulting in GFP-ATG8 signal detection in dotted structures³⁶. In the *Nb/At* interfamily stem-grafts at 14 DAG, GFP fluorescence was particularly showed dotted structure on the scion *Nb* near the graft boundary (Fig. 1e–h). To confirm that these granules are autophagosomes, we verified the localization of GFP-ATG8 by immunoelectron microscopy using anti-GFP and anti-ATG8 antibodies (Supplementary Fig. 1c–f). Signals were observed to be localized to these granules with anti-GFP antibodies (Supplementary Figs. 1c, d). Fewer signals were detected with anti-ATG8 antibody than with anti-GFP antibody, although they were still detected in the granules (Supplementary Figs. 1e, f).

To obtain higher-resolution quantitative observations, we next performed micrografting in the hypocotyl of seedlings, which is a thinner tissue than the stem (Fig. 2 and Supplementary Data 1). The *At* seedlings for the rootstock plants were germinated on a silicone microscaled device, the micrografting chip³⁷ and the *Nb* seedlings for the scion plants were germinated on a nylon blotting membrane on the media, and at 4 days after germination, the hypocotyls of both were cut horizontally and joined on the device (Fig. 2a, b). Even with hypocotyl grafting, the *Nb* scion and the *At* rootstock were able to adhere to the tissues each other within 6 DAG (Fig. 2c, d). We observed by scanning electron microscopy (SEM) that autophagosome formation was visible in hypocotyl grafting as in stem grafting at 5 DAG (Fig. 2e–g). Next, we observed the graft boundary sites at 2, 3, 5, and 14 DAG using ATG8 fluorescence marker lines, since tissue fusion had already begun 2 DAG (Fig. 3 and Supplementary Data 1). Because GFP-ATG8 was introduced into *Nb* and RFP-ATG8 into *At*, each tissue emitted green and magenta fluorescence at background levels in hypocotyls where no grafting treatment was performed (Figs. 3a–d and Supplementary Fig. 2). In both *Nb* and *At* ATG8 marker lines, a small amount of dot-like fluorescence, presumably autophagosomes, was observed in the intact tissue without grafting treatment. However, significantly more autophagosome dots were observed from 2 to 5 DAG in the *Nb* scion than in the intact *Nb* plant (Fig. 3e–m). In contrast, no significant increase of autophagosome dots was observed in the rootstock of the *At* marker line compared to the intact plant (Figs. 3e, g, i, k, n and Supplementary Fig. 2). It is not possible to directly compare the frequency of autophagy occurrence between the *Nb* scion and the *At* rootstock because of the different promoters driving the autophagy marker and the different plant types.

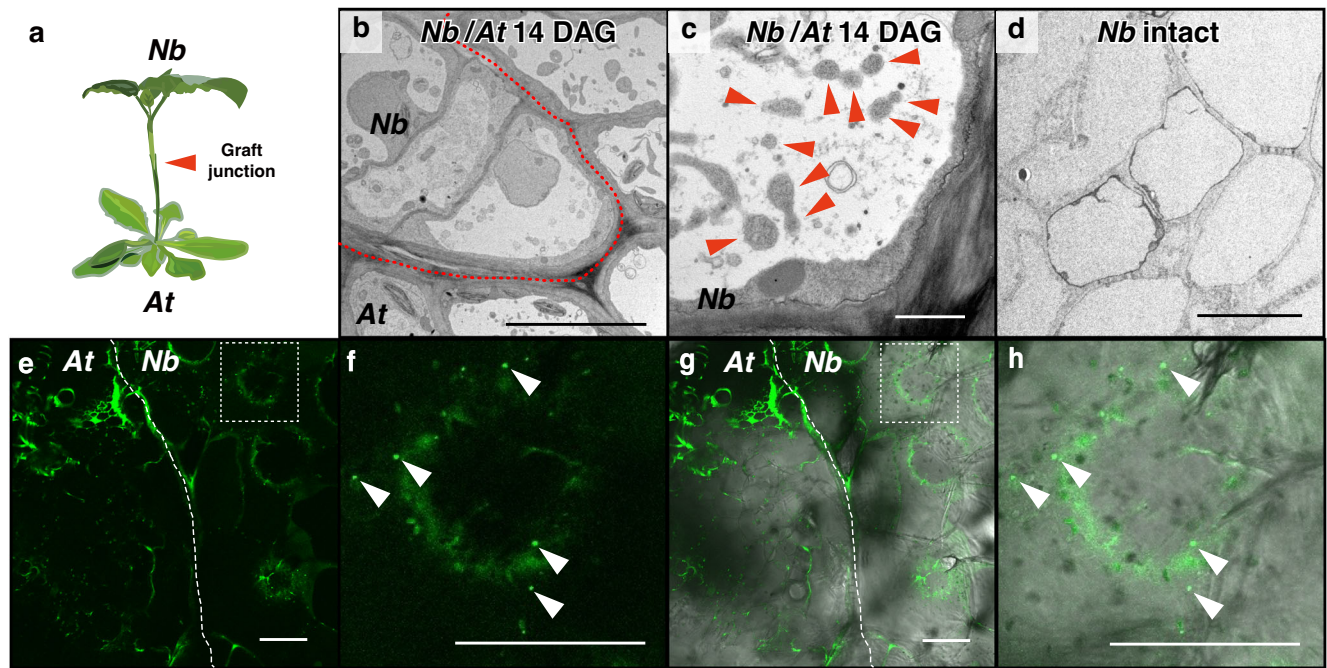


Fig. 1 | Autophagic structures in cells near the graft boundary. **a** Schematic image of *Nb/At* interfamily hetero-graft. **b, c** TEM images of the *Nb/At* hetero-grafts at 14 days after grafting (DAG). Representative images from 5 biological replicates are shown. **b** Image of the boundary cells. **c** Magnified image of a boundary *Nb* cell. **d** TEM images of the cross section of *Nb* intact stem. Representative images from 2 biological replicates are shown. **e–h** GFP fluorescence signals of GFP-ATG8 in

grafting stem of *Nb/At* heterografts at 14 DAG. Representative images from 4 biological replicates are shown. **e, f** GFP signal. **g, h** Merge images of GFP and bright field. **f, h** Magnified images of the squares in (**e, g**). Red and white dashed line indicates the *Nb/At* graft boundary. Red and white arrowheads indicate autophagosomes. Bars = 10 μ m (**b, d**), 5 μ m (**c**) and 100 μ m (**e–h**).

Autophagy was observed in *Nb* homografts

To examine whether the autophagy we have observed is a phenomenon only in grafting of different families, we observed autophagy in the *Nb/Nb* homografts (Fig. 4). *Nb* plants expressing GFP-ATG8 were grafted on day 4 using a micrografting tip device³⁷. Grafting was performed by assembly of the hypocotyl that was cut in the middle of hypocotyl horizontally. Autophagosomes quantification was performed at 2, 3, and 5 DAG and significantly higher GFP-ATG8 fluorescence was observed in the scion region of the *Nb/Nb* homografts at 2 DAG compared to the intact tissues (Fig. 4a–i and Supplementary Data 2). However, the number of autophagosomes in the tissues of the *Nb/Nb* homografts at 3 and 5 DAG was no longer significantly different from the intact plant. The number of autophagosomes in the *Nb* scion of the *Nb/Nb* homograft at 2 DAG was lower than that in the *Nb* scion of the *Nb/At* heterograft at 2 DAG. This may indicate that the healing of the homografts is more rapid than that of heterografts and that autophagy is induced transiently, for several days in homografts, after grafting treatment until accomplishment of tissue healing. The rootstock side of the *Nb/Nb* homograft exhibited no significant autophagy induction. Magnifying the fluorescent image of GFP-ATG8 on the *Nb* scion side of the *Nb/Nb* homograft, we could observe a ring-shaped fluorescence of GFP-ATG8, a characteristic structure of an autophagosome (Fig. 4j). As an autophagosome binds to the vacuole, its inner membrane is released into the vacuole as autophagic body, and the autophagic body is degraded. When degradation of autophagic bodies in the vacuole is inhibited by the treatment of concanamycin A, a V-ATPase inhibitor, fluorescent dots of GFP-ATG8 accumulate in the vacuole. Concanamycin A treated GFP-ATG8 harboring *Nb/Nb* homografts showed numerous GFP-ATG8 derived dot-like structures in the vacuole of the cells in the scion, indicating that the dot-like structure marked by GFP-ATG8 observed here were autophagosomes (Fig. 4k–n).

Autophagy was induced in *At* homografts

Next, we analyzed graft junctions of *At* self-grafting. Since the *Nb/At* hypocotyl micrografting only tested *At* as the rootstock side, we evaluated whether autophagy is induced by grafting in *At* as well. Micrografting was performed on the hypocotyls of *At* seedlings. Hypocotyls were cut horizontally using a micrografting chip to form a flat cut surface. In the *At* homograft, the active formation of autophagic body-like structures in the vacuoles was observed near the graft boundary at 3 DAG (Supplementary Fig. 1g–i) but almost disappeared at 7 DAG (Supplementary Fig. 1j). Magnified TEM images of the graft boundary cells at 3 DAG in *At* homografts showed autophagic bodies in the vacuolar lumen (Supplementary Fig. 1i). SEM images of the *At* hypocotyl homografts showed similar autophagic bodies at 3 DAG (Supplementary Fig. 1k–m).

To monitor autophagy activation in *At* homografts, micrografting experiments were performed using a GFP-ATG8-expressing marker line (Fig. 5 and Supplementary Fig. 3 and Supplementary Data 3). In order to distinguish the boundary region between scion and rootstock, we first used GFP-ATG8 and RFP-ATG8 for grafting combination (Supplementary Fig. 3). However, since the fluorescence intensity of RFP is slightly lower than that of GFP and it is difficult to compare the number of autophagosomes in the scion and rootstock, for quantitative analysis, we used lines expressing ATG8-GFP in both scion and rootstock. GFP-ATG8 was detected at 2, 3, and 5 DAG. At 2 DAG, a significant increase in GFP fluorescence dot structure was observed in the scion part compared to the intact hypocotyl, but not in the rootstock part (Fig. 5a–d, i). In contrast, GFP structures were greatly increased in the scions and were absent in the rootstocks at 3 DAG (Fig. 5e, f, j). Structures with GFP fluorescence remained significantly higher than the intact plant even at 5 DAG (Fig. 5g, h, k), but the extent of those was most remarkable at 3 DAG (Fig. 5i–k). Magnifying the fluorescent image, a characteristic ring-shaped fluorescence of

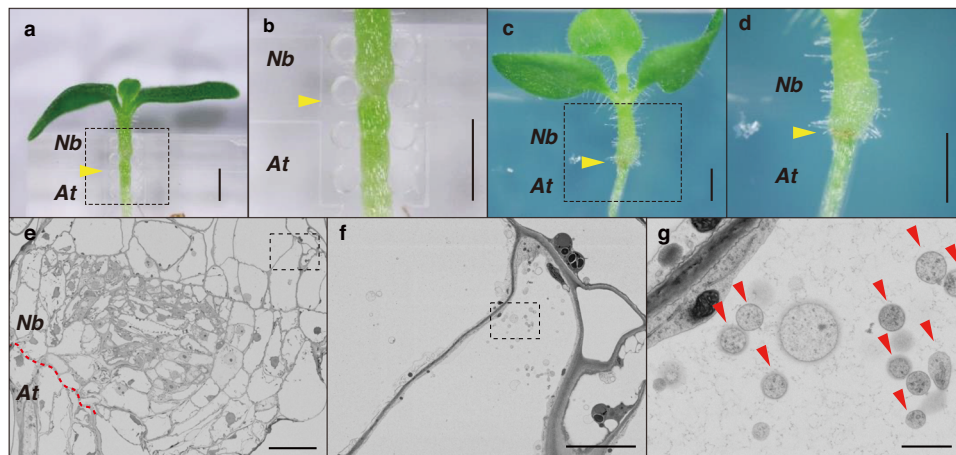


Fig. 2 | Observation of *Nb/At* hypocotyl micrografting. **a–d** Images of the *Nb/At* hypocotyl grafting. **a** An *Nb/At* hypocotyl on the micrografting chip just after grafting. Dashed rectangle indicates the area of **(b)**. **b** A magnified image of **(a)**. **c** An image of *Nb/At* grafted hypocotyl at 6 DAG. Dashed rectangle indicates the area of **(d)**. **d** A magnified image of **(c)**. Yellow arrowheads indicate the grafted position. Bars = 500 μm (**a–d**). **e–g** Autophagic structures in the cells of the *Nb/At* hypocotyl

graft. Images of scanning electron microscopy (SEM) in the *Nb/At* hetero-grafts at 5 DAG. Representative images from 5 technical replicates are shown. **f, g** Magnified images of the area of dashed rectangle in **(e, f)**. The red dashed line indicates the graft boundary. Red arrowheads indicate autophagosomes. Bars = 50 μm (**e**), 10 μm (**f**) and 1 μm (**g**).

autophagosome was observed in the *At/At* homografts (Fig. 5l). Moreover, concanamycin A treated *At/At* homografts exhibited high number of the GFP fluorescence signals in the vacuole (Fig. 5m–p). Autophagic bodies were released into the vacuole and, as results, the fluorescence of GFP-ATG8 appeared in dots drifting within the vacuole (Supplementary video1). To further examine induction of autophagy during grafting, Western blotting analysis was performed to see an occurrence of GFP-ATG8 protein digestion after translocation to vacuole through autophagy mechanism. Intact and grafted plants were examined using a GFP antibody for GFP-ATG8 protein detection (Fig. 5q). In plants, ATG8 located in the inner membrane of the autophagosome is degraded after uptake into the vacuole. Yet, in the case of GFP-bound ATG8 protein, the portion of GFP with the barrel structure is relatively stable even in the vacuole and accumulates in the vacuole in a free state²⁶. Therefore, free GFP is detected by western blotting when autophagy is triggered. Free GFP was barely detectable in intact *At* plants but accumulated from 1 DAG in homografted *At*, reaching 5.11-fold at 3 DAG and maintaining its accumulation until 7 DAG (Fig. 5q). These results indicate that autophagy is triggered in homografting of *At* as well as *Nb*.

Grafting is considered to be a particular form of wound repairing. In some cases, wound repairing only involves sealing the wound surface without connecting the wounds back together. To determine the triggering factor for autophagy induction during grafting, we maintained the cut surface of the hypocotyls of *At* plants apart after cutting and detected GFP-ATG8 (Supplementary Fig. 4). The GFP-ATG8 dot signal accumulated significantly at the hypocotyl end, corresponding to the upper scion from the cleavage site. In contrast, no difference was observed at the hypocotyl end corresponding to the rootstock below the cleavage site compared with the intact hypocotyl. This indicated that autophagy was primarily induced by cleavage without entering to the stage of tissue adhesion by grafting.

Autophagy contributed to wound healing in homo-grafting

To explore whether autophagy is critical for graft establishment and wound repair, graft healing experiments were performed using *atg* mutants of *At*. ATGs were divided into four categories based on the human autophagy pathway in the KEGG PATHWAY (has04136): the ATG1 protein kinase complex (ATG1, ATG11, ATG13, ATG101), which is the first response to nutrient starvation; the membrane delivery complex of ATG2, ATG9 and ATG18; PI3K complex (ATG6); and the

large system including the ubiquitin-like reaction system (ATG3, ATG4, ATG7, ATG10), ATG12 conjugation system (ATG5, ATG12, ATG16), and the ATG8 lipidation system (Supplementary Fig. 5 and Supplementary Data 4). We analyzed the loss-of-function mutants of two genes; ATG2, which functions in membrane delivery, and ATG5, which functions in the ATG12 conjugation system.

Using *At atg2* and *atg5* mutants, *At/At* micrografting was conducted between the *atg* mutant scion and the WT rootstock. The graft success rate of the *atg5* scion was significantly decreased ($P < 0.05$, χ^2 test) (Fig. 6a and Supplementary Data 5), whereas that of the *atg2* scion decreased but not significantly (Supplementary Fig. 6a and Supplementary Data 5). For the *atg2* mutant analysis, we measured the fresh weight of shoot of intact and grafted plants an indicator of graft healing⁴ (Supplementary Fig. 6b,c and Supplementary Data 6). The *atg2* mutant showed a slight but significant decrease in the shoot fresh weight compared to the WT at 7 days after germination (Supplementary Fig. 6b). Therefore, we performed WT/WT and *atg2*/WT grafts and calculated the relative value of “the shoot fresh weight of the grafted plants” to “the shoot fresh weight of the corresponding intact plants”. Since primary vascular formation starts around after 3 DAG in *At/At* micrografting and the growth of grafted plants is arrested at least 3 days after grafting, we estimated that the growth state of 7-day-old intact plants approximately corresponds to that of grafted plants at 10 DAG, and collected data at these time points. The relative value of shoot fresh weight of the *atg2* scion to intact *atg2* mutant showed a significant decrease rather than that of the WT scion to intact WT plant (Supplementary Fig. 6c and Supplementary Data 6).

ATG5 contributed to wound healing in interfamily hetero-grafting

We examined the role of autophagy in *Nb/At* interfamily heterografting by conducting virus-induced gene silencing (VIGS) experiments^{4,38} focusing on *NbATG5* (*Nbe.v1.1.chr12g36840.1*). *Nb* has two homologs corresponding to *AtATG5* (*ATSG17290*), but one gene (*Nbe.v1.1.chr02g25660.1*) was scarcely expressed in the graft region (Supplementary Data 7). A scion from an *Nb* plant in which *NbATG5* was knocked down using the VIGS system (*NbATG5* VIGS) was grafted onto an *At* bolting stem and the survival rate was determined at 14 DAG. As controls, scions from non-infected (NI) *Nb* plants or those infected with *CMV* expressing a fragment of the GFP sequence (*GFP* VIGS) were grafted onto *At* rootstocks. First, we confirmed the suppression of

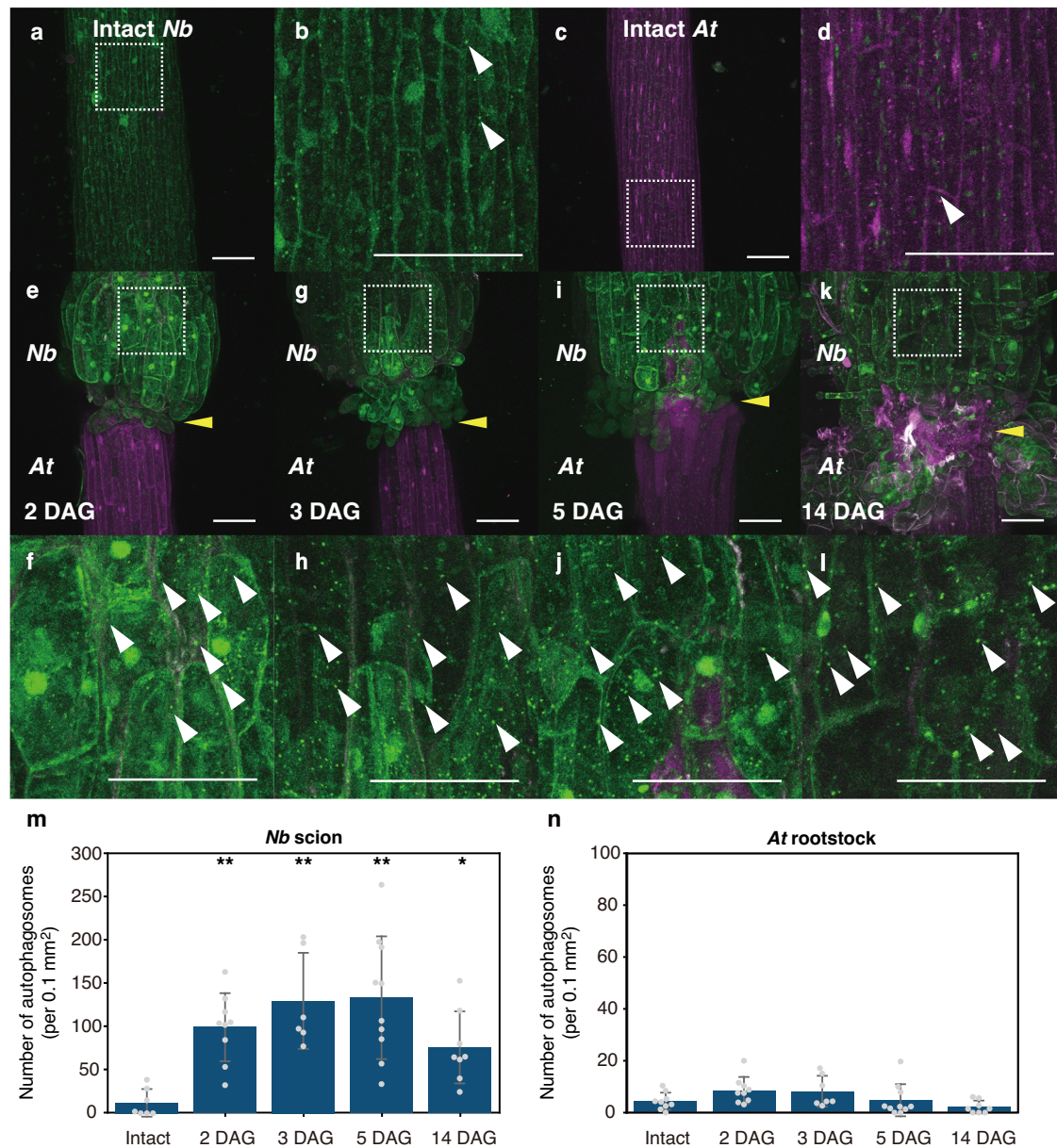


Fig. 3 | GFP-ATGS observation of *Nb/At* hypocotyl micrografting. **a–l** GFP and RFP fluorescence signals detected in the intact *Nb* and *At* and the *Nb/At* heterografted hypocotyls with a confocal laser scanning microscope. **a, b** GFP fluorescence image in the intact *Nb* hypocotyl. **c, d** RFP fluorescence image in the intact *At* hypocotyl. **e–l** Merged fluorescence images of GFP and RFP in the *Nb/At* grafted hypocotyls observed at 2 (**e, f**), 3 (**g, h**), 5 (**i, j**), and 14 DAG (**k, l**). **b, d, f, h, j, l** Magnification images of (**a, c, e, g, i, k**). Dashed rectangles in (**a, c, e, g, i, k**) indicate the areas of (**b, d, f, h, j, l**), respectively. Yellow arrowheads indicate the grafted positions. White arrowheads indicate examples of autophagosomes. Not all

autophagosomes are indicated. Bars = 100 μ m. **m, n** Quantification of autophagosomes in the image of maximum intensity projections of the intact *Nb* (**a**), the intact *At* (**c**), and the *Nb* scion and *At* rootstock (**e, g, i, k**). Error bars represent standard deviation. Asterisks indicate statistically significant differences compared with intact hypocotyls as determined by one-way analysis of variance (ANOVA; $P < 0.05$) followed by Dunnett's multiple comparison test ($* P < 0.05$, $** P < 0.01$). Sample sizes: (**m**): Intact ($n = 7$), 2 DAG ($n = 9$), 3 DAG ($n = 6$), 5 DAG ($n = 10$), 14 DAG ($n = 8$); (**n**): Intact ($n = 9$), 2 DAG ($n = 9$), 3 DAG ($n = 7$), 5 DAG ($n = 10$), 14 DAG ($n = 8$). All experiments were independently performed twice with similar results.

NbATG5 expression using VIGS using tissue samples from the graft junction at 3 DAG (Fig. 6b and Supplementary Data 8). The survival rate at 14 DAG of the *NbATG5* VIGS heterografts was significantly lower than that of the NI or *GFP* VIGS heterografts (Fig. 6c and Supplementary Data 8). These results suggested that *NbATG5* plays a role in the establishment of *Nb/At* interfamily heterografts.

Grafting caused nutrient deficiency

Based on previous reports that nutrient starvation induces autophagy²⁶, we hypothesized that autophagy activation after grafting is induced by nutrient starvation because the grafting procedure

involves temporary cessation of nutrient transport in the vascular tissues connecting the shoot and root. We examined the extent of mass flow from the rootstock to the scion and gene expression at the graft junction in *Nb* homografts and *Nb/At* interfamily heterografts (Fig. 7a, b).

To monitor the mass transport from the rootstock to the scion, we applied a radioisotope species, ³²P, to the rootstock of *Nb/Nb* homografts and *Nb/At* heterografts at 3 and 7 DAG, and isotope signals were subsequently detected in the scions (Methods and Supplementary Fig. 7). The intact *Nb* plants were treated in the same manner as the control experiment. In intact *Nb* plants, Pi uptake from the stem is

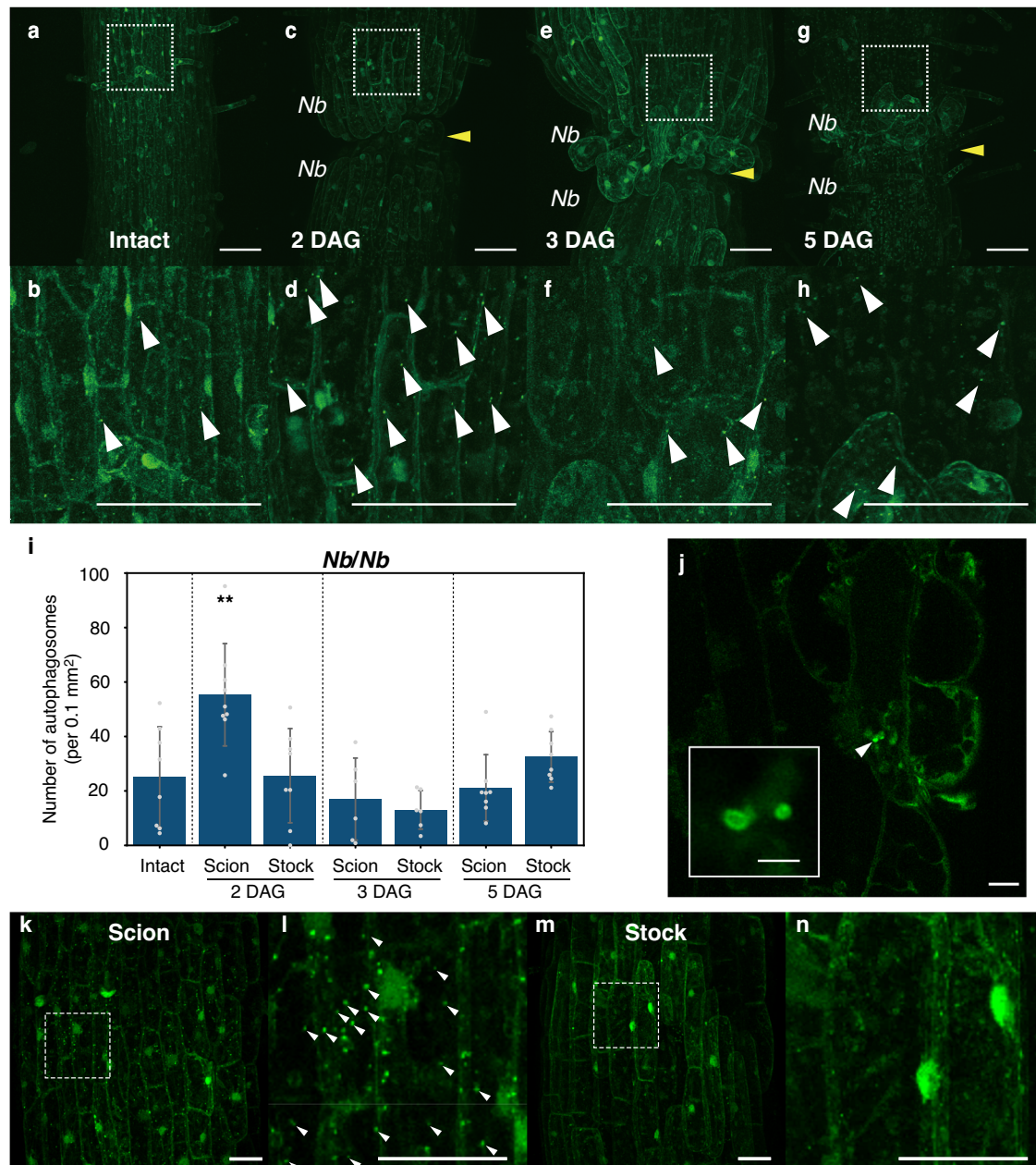


Fig. 4 | GFP-ATG8 observation in *Nb/Nb* hypocotyl homo-grafting.

a–h Representative GFP fluorescence signals detected in grafting of *Nb* hypocotyls of GFP-ATG8 plants with a confocal laser scanning microscope. Maximum intensity projections of z-stacks. **a, b** Intact *Nb*. **c, d** 2 DAG. **e, f** 3 DAG. **g, h** 5 DAG.

b, d, f, h Magnification images of (**a, c, e, g**). Yellow dashed lines indicate the grafting boundary. White arrowheads indicate autophagosomes. Bars =100 μ m.

i Quantification of autophagosomes in the image of maximum intensity projections of (**a, c, e, g**). Error bars represent standard deviation. Asterisks indicate statistically significant differences compared with intact hypocotyls as determined by one-way ANOVA ($P < 0.05$) followed by Dunnett's multiple comparison test (** $P < 0.01$). Sample sizes: Intact ($n = 8$); 2 DAG: Scion ($n = 9$), Stock ($n = 9$); 3 DAG: Scion ($n = 6$),

Stock ($n = 6$); 5 DAG: Scion ($n = 8$), Stock ($n = 8$). **j** Fluorescent image of GFP-ATG8 observed in a ring shape, a characteristic structure of autophagosome, in the scion of the *Nb/Nb* graft. Bar =100 μ m. A magnified image of the bright spot pointed by the arrowhead is shown in inset. Bar =20 μ m. **k–n** Accumulation of GFP-ATG8 vesicles in the vacuoles upon concanamycin A treatment in the *Nb/Nb* grafts expressing GFP-ATG8. **k, l** Images of the scion side of the grafted hypocotyl. **m, n** Images of the rootstock side of the grafted hypocotyl. Dashed rectangles in (**k, m**) indicate the areas of (**l, n**), respectively. White arrowheads indicate autophagic body in the vacuoles. Bars =100 μ m (**k, m**) and 50 μ m (**l, n**). All experiments were performed three times independently.

rapidly transported to the leaves, so the isotope signal was strongly detected in the leaves (Fig. 7a). In both homo- and hetero-grafts at 3 DAG, the isotope signals in leaves were only detected at very low intensity compared to intact *Nb* (Figs. 7a, b, Supplementary Fig. 7 and Supplementary Data 9). However, at 7 DAG, the signal remained low in the *Nb/At* heterografts, whereas in the *Nb/Nb* homografts, the signal increased to almost the same level as in the intact *Nb* plants (Figs. 7a, b, Supplementary Fig. 7 and Supplementary Data 9). These results

indicate that Pi movement from root or stem to leaf is once blocked by grafting treatment, but is gradually restored if homo-grafting. In hetero-grafting, however, the recovery was suggested to be much delayed compared to homo-grafting.

Next, we examined the expression levels of marker genes in response to mineral nutrient starvation stress. *Nb* homologs have been identified in genes responsive to phosphorus and nitrogen deficiencies in *At*^{39–41}. In our transcriptome data for *Nb/At* interfamily heterografts⁴,

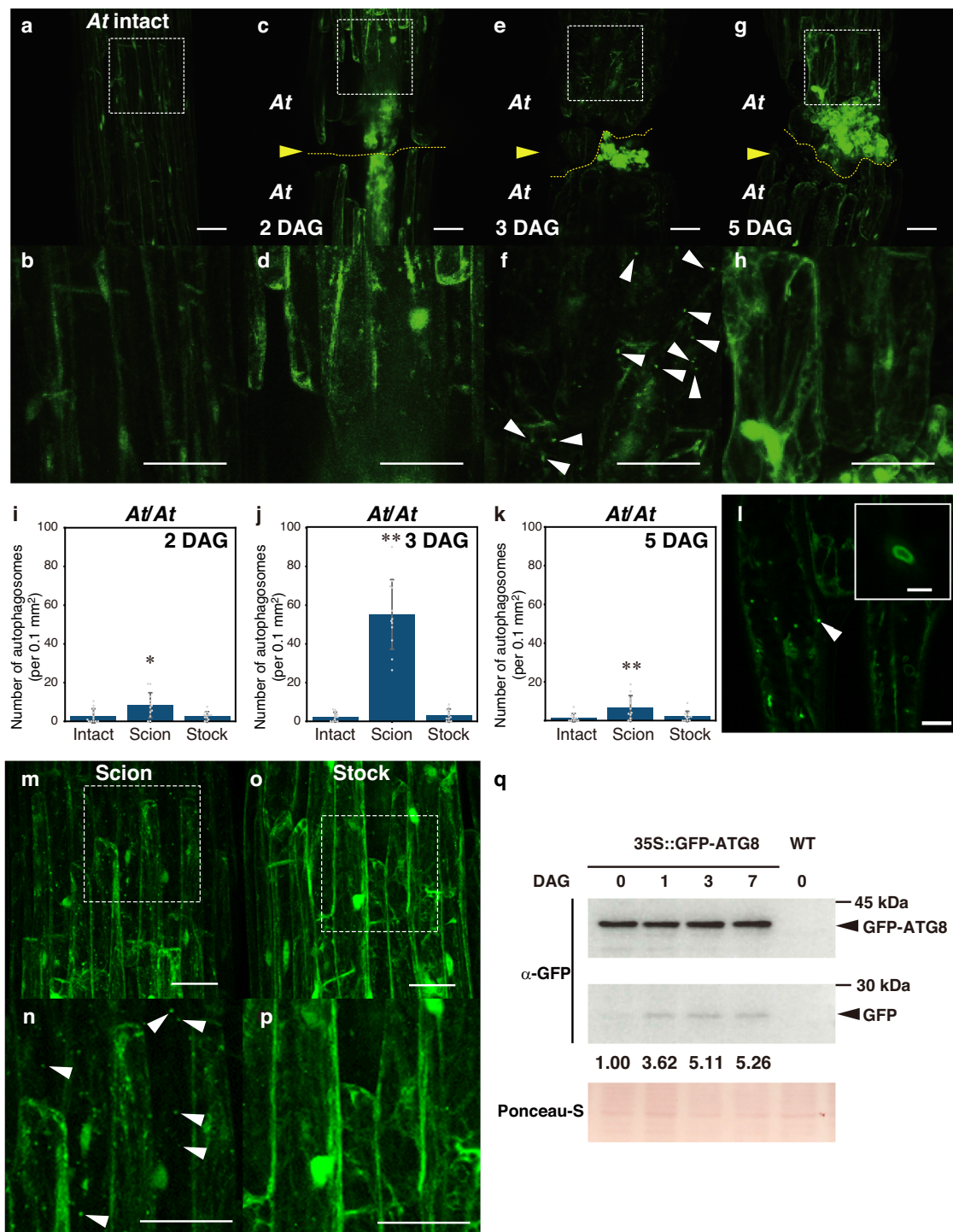


Fig. 5 | GFP-ATG8 observation in *At/At* homo-grafting. **a–h** Representative GFP fluorescence signals detected in grafting of *At* hypocotyls of GFP-ATG8 plants with a confocal laser scanning microscope. Maximum intensity projections of z-stacks. **a,b** Intact *At*. **c,d** 2 DAG. **e,f** 3 DAG. **g,h** 5 DAG. **b, d, f, h** Magnification images of dashed rectangle areas in (**a, c, e, g**). Yellow dashed lines indicate the grafting boundary. White arrowheads indicate autophagosome points. Bars = 50 μ m. **i–k** Quantification of autophagosomes in the image of maximum intensity projections of (**a, c, e, g**). Error bars represent standard deviation. Asterisks indicate statistically significant differences compared with intact hypocotyls as determined by one-way ANOVA ($P < 0.05$) followed by Dunnett's multiple comparison test (* $P < 0.05$, ** $P < 0.01$; $n = 12$). **l** Fluorescent image of GFP-ATG8 observed in a ring shape, a characteristic structure of autophagosome. Bars = 100 μ m. A magnified image of the bright spot pointed by the arrowhead is shown in inset. Bar = 20 μ m.

m–p Accumulation of GFP vesicles in the vacuoles upon concanamycin A treatment. **m, n** Images of the scion side of the grafted hypocotyl. **o, p** Images of the rootstock side of the grafted hypocotyl. Dashed rectangles in (**m, o**) indicate the areas of (**n, p**), respectively. White arrowheads indicate autophagic body in the vacuoles. Bars = 100 μ m (**m, o**) and 50 μ m (**n, p**). **q** Representative data of ATG8 cleavage in *At* hypocotyl grafting using an anti-GFP antibody. The top panel shows the signal corresponding to GFP-ATG8 and the middle panel shows the ATG8-cleaved GFP signal. The bottom panel shows a membrane-stained image with Ponceau S to ensure uniformity of loading. The numbers at the bottom of the middle panel show the relative intensity of ATG8-cleaved GFP at each time when the signal intensity of intact is set to 1.00. All experiments were performed three times independently.

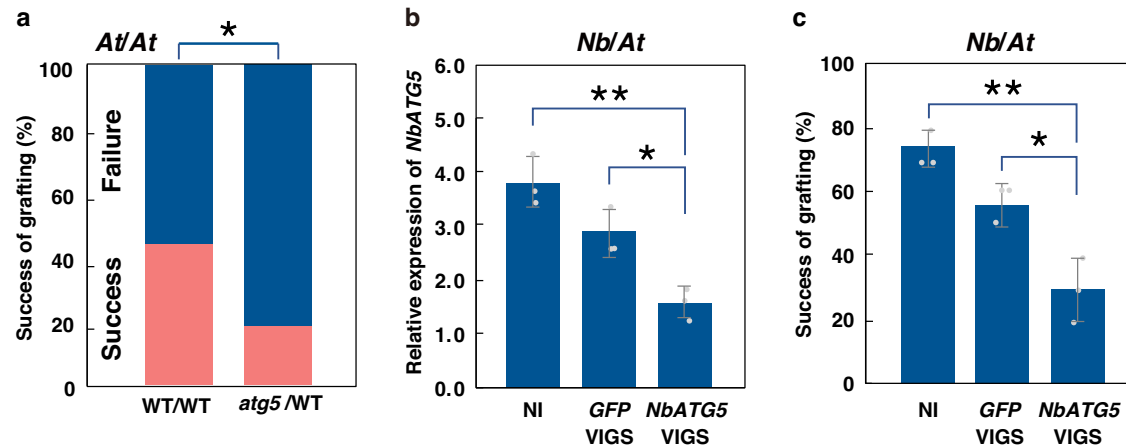


Fig. 6 | Autophagy contributed to wound healing in *At/At* homo- and *Nb/At* hetero-grafting. **a** Success rate of WT and *atg2* mutant grafts onto WT rootstock at 14 DAG. Error bars represent standard deviation. Asterisk indicates a statistically significant difference as determined by χ^2 test ($*P < 0.05$; $n = 81$ and 38 for WT/WT and *atg5*/WT, respectively). **b, c** VIGS experiment targeting *NbATG5* was performed in the *Nb/At* stem grafting. **b** Suppression of *NbATG5* expression by VIGS was verified by qRT-PCR (three grafts were conducted for each sample fraction). Expression levels were normalized against the reference gene *NbACT1* and adjusted to be

relative to the sample with no virus infection (NI). Error bars represent standard deviation. Asterisks indicate statistically significant differences as determined by two-way ANOVA ($P < 0.05$) followed by Tukey's post-hoc test ($*P < 0.05$, $**P < 0.01$; $n = 3$). **c** Effect of suppression of *NbATG5* expression by VIGS on graft establishment. Experiments were performed three times. For each experiment, 10 grafts were conducted for each sample fraction. Asterisk indicates a statistically significant difference as determined by χ^2 test ($*P < 0.05$, $**P < 0.01$).

the upregulation of many of these genes was detected (Figs. 7c and Supplementary Data 10). The transcriptome data for *Nb* homo-grafted samples also showed a tendency for increased gene expression levels at 1 and 3 DAG. However, the expression levels of these genes at 7 DAG did not increase compared to those in the *Nb/At* heterografts. We further confirmed the expression of *Nbe.v1.1.chr19g26790.1*, *Nbe.v1.1.chr07g07060.1*, and *Nbe.v1.1.chr18g24590.1*, the *Nb* homologs of *EARLY RESPONSE to DEHYDRATION STRESS5 (ERDS)*, *suppressor of the G2 allele of skp1 (SGT1)*, and *NITRATE TRANSPORTER2.5 (NRT2.5)*, respectively, which are nutrient deficiency-responsive genes in *At*. The expression of these three genes at 1, 3, and 7 DAG in *Nb* homografts and *Nb/At* interfamily heterografts and their expression in intact plants was quantified using quantitative reverse transcription PCR (qRT-PCR) (Supplementary Fig. 8a). The degree of increase for all three genes was greater in the *Nb/At* interfamily heterografts. The expression gradually increased from 1 to 7 DAG, indicating that the interfamily heterografts experienced more severe stress than the homografts. Note that the nutrient deficiency responses in gene expression were also observed in the *At* rootstock side of the *Nb/At* interfamily heterografts (Supplementary Fig. 8b). This was possibly due to the fact that the nutrient supply on the rootstock side, which is connected to the source of inorganic nutrients, is also reduced because the transpiration flow is stopped by the breaks in the vascular tissues. In TEM images of the *Nb/At* stem grafts, many autophagic body-like structures were also observed in cells on the *At* side of the rootstock, possibly indicating that autophagy is induced on the rootstock side in interfamily stem-grafting (Fig. 1b). Thus, it was suggested that the grafting sites remained nutrient deficient until graft reconnection. Interfamily heterografts are subjected to severe and prolonged nutrient-deficient conditions.

Autophagy is required for wound-induced callus formation under nutrient starvation

Callus is a cluster of unorganized, randomly formed plant cells. Callus is composed of dedifferentiated cells, most of which are differentiated pluripotent and capable of regenerating even whole plants. Wounded plant causes rapid callus formation from the wound site⁴². Alternatively, grafted plant causes callus formation from the cambium at the junction, which first fills the gap between the scion and rootstock (Supplementary

Fig. 9). In addition, callus can be artificially induced from plant tissue by the administration of plant hormones. Recently, it was reported that callus formation induced by such hormones is reduced in the root tissues of *At atg* mutants⁴³. In this study, we focused on wound-induced callus, which was observed in the early stage of graft establishment, and investigated whether the callus formed on the cut surface of the hypocotyl under conditions without the addition of phytohormones was affected by the *atg* mutation. The *atg2* and *atg5* hypocotyls were cut and cultured on medium, and callus formation on the cut surface of the hypocotyl piece was observed at day 11. Since it was suggested that autophagy may be induced by the lack of nutrients in the graft, we cultured the grafted plants on a medium lacking carbon or nitrogen, or both of them. The frequency of callus formation and callus size were compared with those of the WT, and it was found that callus formation was significantly inhibited in both *atg2* and *atg5*, especially when they were placed on carbon-deficient medium (Figs. 7d–h and Supplementary Data 11). Nitrogen deficiency also affected both callus formation frequency and callus size in the *atg* mutant, but carbon deficiency was more pronounced. The effects of deficiency of the two elements were synergistic. The *atg5* had lower callus formation frequency and callus size than WT even under adequate nutritional conditions, but the effect was more severe with carbon deficiency.

An energy-producing pathway for carbon deficiency includes an alternative respiratory pathway for amino acid-derived ATP production in mitochondria. Autophagy is known to be involved in the generation of amino acids to this pathway⁴⁴. We verified whether this pathway is involved in the formation of hypocotyl callus by adding casamino acids, the mixture of amino acids and small peptides derived from acid hydrolysates of casein, to a carbon-deficient conditioned medium. The reduction of callus formation under carbon deficiency in the *atg2* and *atg5* mutants was restored by the addition of casamino acids (Figs. 7i, j and Supplementary Data 12). This observation suggests that during carbon deficiency, an alternative respiratory pathway for ATP production occurred by autophagy-driven amino acid supply through and promoted callus formation at the wound surface.

Discussion

Autophagy is a nutrient-recycling response triggered by internal and external stresses in plants. This study identified autophagy activation

Fig. 7 | Autophagy was required for callus formation under nutrient-deficient conditions. **a** Phosphorus transport in an intact *Nb* plant, an *Nb/At* homo-graft and an *Nb/At* hetero-graft. All plantlets incorporated inorganic phosphate (Pi) labeled with ^{32}P from the cut stems. The signal amount is shown as a heat map; the gradient from white to blue corresponds to higher to lower signals. Insets indicate the reference points to compare the signal intensity. Arrowheads indicate the grafted position. Bars = 5 cm. **b** Quantification of Pi transport by imaging plates at 6 h after application. Error bars represent standard deviation. Differences between the sample groups were tested using two-way ANOVA followed by a Tukey's post-hoc test ($P < 0.01$; biological replicates: $n = 13, 13$ and 11 for intact *Nb*, *Nb/Nb* and *Nb/At* in 3 DAG, and $11, 12$ and 13 for intact *Nb*, *Nb/Nb* and *Nb/At* in 7 DAG, respectively). **c** Expression levels of genes responsive to nutrient starvation. The expression levels of *Nb* genes were established by transcriptomic analysis of the intact *Nb*, *Nb/Nb*, and *Nb/At* grafted samples. **d–f** Callus formed at the lower end of the cut hypocotyl under carbon-deficient conditions in wild type (**d**), *atg2* (**e**) and *atg5* (**f**). The hypocotyls were cut at 7 days after germination and cultured for 11 days on MGRL medium without sucrose as carbon source. Experiments were performed three times. For each experiment, 30 seedlings were observed. Bars = 200 μm . **g** Frequency of callus formation in wild type, *atg2*, and *atg5* plants grown for 11 days after hypocotyl cutting on normal MGRL medium, carbon-depleted (-C), nitrogen-depleted (-N), and both carbon and nitrogen-depleted (-C-N) MGRL medium. Three independent trials were averaged. Error bars represent standard deviation. Asterisks indicate statistically significant differences compared with WT as determined

by one-way ANOVA ($P < 0.05$) followed by Dunnett's multiple comparison test ($*P < 0.05$, $**P < 0.01$; $n = 3$). **h** Total area of callus formed per plant in wild type, *atg2* and *atg5* cultured for 11 days after hypocotyl cutting on normal MGRL medium, carbon-depleted (-C), nitrogen-depleted (-N), and depleted of both carbon and nitrogen (-C-N) MGRL medium. The numbers in the graph indicate the number of outliers above the scale. Error bars represent standard deviation. Asterisks indicate statistically significant differences compared with WT as determined by one-way ANOVA ($P < 0.05$) followed by Dunnett's multiple comparison test ($*P < 0.05$, $**P < 0.01$; $n = 79, 71$ and 64 for WT, *atg2* and *atg5* in +NC, $86, 47$ and 54 for WT, *atg2* and *atg5* in -C, $77, 62$ and 63 for WT, *atg2* and *atg5* in -N, $55, 35$ and 43 for WT, *atg2* and *atg5* in -C-N). **i, j** Comparison of callus formation frequency (**i**) and the area of callus formed per plant (**j**) in wild type, *atg2* and *atg5* cultured for 11 days after hypocotyl cutting on carbon deficient MGRL medium (blue) and carbon deficient MGRL medium supplemented with 0.1 g/L casamino acid (right blue). A box plot represents the interquartile range from the first quartile to the third quartile. The horizontal line inside the box indicates the median. The whiskers extend to cover 95% of the data range. The number of outliers that fell outside the plot frame is indicated at the top of each graph. Error bars represent standard deviation. Asterisks indicate statistically significant differences in Student's T test ($*P < 0.05$, $**P < 0.01$; $n = 3$ for (**i**), $n = 67, 75, 36, 64, 29$ and 57 for WT (-C), WT (-C + A), *atg2* (-C), *atg2* (-C + A), *atg5* (-C) and *atg5* (-C + A) in (**j**)). **k** Model for wound healing processes in grafting.

response, nutrient and hormonal regulation, cell regeneration, and tissue reunion through cell differentiation for each required cell type. Some critical knowledge gaps remain, such as the means of recognizing a grafting partner that may reflect graft compatibility. In normal compatible grafting, such as homografting, callus formation occurs at the grafting boundary within 2–3 days after grafting and extends until accomplishment of graft union formation (Supplementary Fig. 9a). Post-grafting growth was also suppressed in these mutants and a reduced grafting success rate was observed for *Atatg5* and *NbATG5* VIGS (Fig. 5f–h). Wounding and grafting cause the vascular bundles to break off (Supplementary Figs. 9b, c). This may stop the supply of inorganic nutrients through the xylem from the root to the shoot and reduce the translocation of carbon sources from the leaves to the cut site because of the rupture of the phloem. Autophagic cellular recycling systems may complement the nutrient deficiencies that inhibit callus formation at injured and grafted sites.

In quantitative observations using lines expressing the fluorescent protein fusion-ATG8, autophagosomes were observed in cells on the scion side in the *Nb/At*, *Nb/Nb*, and *At/At* hypocotyl grafts (Figs. 3–5 and Supplementary Fig. 2, 3). Previous reports on plant wound repairing suggest that the non-uniform distribution of auxin caused by wounds triggers the expression of *ANAC71* in the upper part of the wound and *RAP2.6L* gene in the lower part of the wound, and that different repair mechanisms are activated in the wounded sites⁴⁵. *WOUND-INDUCED DEDIFFERENTIATION (WIND) 1–4* have been reported to function upstream of the cytokinin pathway during wound stress-induced callus formation⁴⁶. The balance between auxins and cytokinins may affect callus formation. It is not clear at this time whether autophagy has a direct relationship to these hormone balances. *WUSCHEL-RELATED HOMEBOX 13 (WOX13)* in *At* is rapidly induced by wounding and is partly dependent on WIND1 activity. *WOX13* upregulates the expression of *WIND2* and *3*. *WOX13* also regulates the transcriptional induction of cell wall modification enzyme genes, such as *GLYCOSYLHYDROLASE9Bs*, *PECTATELYASE LIKEs*, and *EXPANSINs*^{47,48}. These insights suggested that active callus formation and subsequent tissue reunion were regulated by the same grafting pathways in particular.

A series of observations implies that, compared to *Nb/Nb* and *At/At* homografts, *Nb/At* heterografts join tissues less effectively. During the *Nb/At* stem grafting, Pi transport from the rootstock to the scion was limited even at 7 DAG (Fig. 7a, b). In the hypocotyl grafting, transient autophagosomes were observed from 2 to 3 DAG in the

Nb/Nb and the *At/At* homografts, whereas autophagosome accumulation was observed continuously up to 14 DAG in the *Nb/At* heterografting. A recent report demonstrated that heterografts of *Solanum lycopersicum* and *Capsicum annum* showed signs of anatomical junction failure within one week after grafting. Gene regulatory network estimation of graft-compatible self-grafts and non-compatible heterografts showed that *SIWOX4*, as a core regulator of grafting, is essential for vascular reconnection during grafting and may serve as an early indicator of graft failure⁴⁹. In our previous study, we showed that after an initial wound response upon grafting, severed tissue healed via the action of glycosyl hydrolase 9B3, followed by the induction of *XYLEM CYSTEINE PEPTIDASE 1* expression by *VASCULAR RELATED NAC-DOMAIN PROTEIN 7*, which promoted the neogenesis of tracheary elements and joining of xylems^{4,34}. Autophagy activation during grafting occurred transiently around tissue fusion and the xylem junction. From these facts, we propose a model. First, the stem tissue injury associated with grafting restricts the movement of nutrients, resulting in a state of nutrient starvation. This leads to an increase in gene expression in relation to nutrient starvation and induction of autophagy in the grafting area. Here, autophagy induction is more conspicuous on the grafted scion side. Callus formation is promoted by energy supplementation through autophagy functions. The callus fuses the cellular tissues of the scion and rootstock. The vascular tissue is reconstructed accordingly (Fig. 7k). The relationship between these grafting events and the triggering of autophagy is not yet well understood and requires further study.

Methods

Plant materials

Arabidopsis thaliana (*At*) ecotype Columbia (Col) was used as WT. The *At atg2* (*atg2-1*, SALK_076727) and *atg5* (CS39993) mutant lines were obtained from the Arabidopsis Biological Resource Center (<http://www.arabidopsis.org/abrc>). The *At* GFP-ATG8 line used in this study has been described by Yoshimoto et al.³⁵. *At* and *Nicotiana benthamiana* (*Nb*) seeds were surface sterilized with 5% (w/v) bleach for 5 min, washed three times with sterile water, incubated at 4 °C for 3 days, and planted on a medium containing half-strength Murashige and Skoog (1/2 MS) medium, 0.5% (m/v) sucrose, and 1% agar. The pH was adjusted to pH 5.8 with 1M KOH. For callus formation observation, Molecular genetics research laboratory (MGRL) medium was used with no sucrose added for carbon deficiency and $\text{Ca}(\text{NO}_3)_2$ and KNO_3 replaced by CaCl_2 and K_2SO_4 for nitrogen deficiency⁵⁰. Seedlings were

grown at 22 °C for *At* and 27 °C for *Nb* and 100 $\mu\text{mol m}^{-2} \text{s}^{-1}$ of illumination under continuous light conditions.

Grafting experiments

Nb/At stem grafting was performed as described by Okayasu and Notaguchi⁵¹. Briefly, the stems of 4-week-old *Nb* were wedge-grafted onto the bolting stems of 5-week-old *At* plants. This procedure was the same for the *Nb* homograft and *Nb/At* heterograft in plants of the same age. *At* micrografting was performed using a supportive microdevice, a micrografting chip developed by Tsutsui et al.³⁷. Seeds were sown in a prescribed seed pocket of the chip and the chips were placed on a Hybond-N+ nylon membrane (GE Healthcare, Chicago, IL, USA), which was placed on 1/2 MS medium containing 1% sucrose and 1% agar. Four-day-old seedlings were then subjected to micrografting. In this system, both the rootstock and scion hypocotyls were cut horizontally with a knife (Kai Co., #2-5726-22 No.11, Tokyo, Japan) and assembled on the chip using forceps. A groove structured on the chip allowed us to cut the hypocotyl smoothly using a knife to create a fine, flat graft surface. Two micropillar arrays on the chip supported the hypocotyls of both the rootstock and scion, resulting in uniformly constructed micrografted plants. After grafting, the plants were transferred to a new 1/2 MS medium containing 2% agar and grown at 27 °C for 6 days, transferred to a new 1/2 MS medium containing 1% agar and grown at 22 °C for 4 days. This corresponded to 10 DAG, when the phenotype was examined. The detailed procedures are described in Tsutsui et al.⁵². This procedure was the same for the *Nb* homograft and *Nb/At* heterograft in plants of the same age.

Radioisotope transport assay

Intact *Nb* plants, *Nb* homografts, and *Nb/At* heterografts were used in radioisotope experiments. All leaves except for 3–4 pieces of leaves in intact or scion plants were removed and the stem was cut at its base and placed in a 5-ml tube containing 2 ml of distilled water, inorganic phosphate (Pi; 0.1 μM), and ³²P-phosphate (10 kBq). After 6 h incubation at 27 °C, ³²P distribution in the plant was visualized using radioluminography with an imaging plate (GE Healthcare UK, Amersham, UK) and an FLA-5000 image reader (Fujifilm, Tokyo, Japan). The amount of ³²P was calculated using an image analysis software (Image Gauge 4.0, Fujifilm). For the time-course analysis, we employed the Real-Time Radioisotope Imaging System developed by Sugita et al.⁵³, which enabled us to sequentially observe ³²P distribution in the plant. The activity of ³²P-phosphate in the incubation solutions was 30 kBq for *Nb* and *Nb/Nb* and 60 kBq for *Nb/At*. Radioactivity images were captured during the dark period of a 15-min light/dark cycle. The accumulation of ³²P in the scion and rootstock was examined in two segments (10 × 10 cm) collected above and below the graft union.

Transcriptome analysis

RNA sequencing was conducted on sequential samples of grafted regions on stems as described previously. To graft samples of *Nb* and *At*, the sequence reads were mapped to the genome assembly using HISAT2 version 2.1.0 (<http://daehwankimlab.github.io/hisat2/>). Gene expression levels, expressed as fragments per kilobase of transcript per million fragments mapped (FPKM), were estimated using the Cufflinks software (version 2.1.1; <http://cole-trapnell-lab.github.io/cufflinks/>). The reference sequences used for mapping and annotation files were the *N. benthamiana* draft genome sequence v1.0.1 (<https://btscience.org/our-research/research-facilities/research-resources/nicotiana-benthamiana>) and *A. thaliana* TAIR10 genome release (<https://www.arabidopsis.org>).

Western blotting

Total protein was extracted from the graft region of the *At* GFP-ATG8 homografts using 1×PBS buffer. One sample was prepared by

collecting twenty intact or grafted hypocotyls region, from approximately 1 mm above the graft surface to approximately 1 mm below the graft surface. The samples were incubated at 100 °C for 3 min. The supernatants were obtained by centrifugation at 15,000 × *g* at 4 °C for 1 min. The supernatants were adjusted to 1×SDS loading buffer and resolved on SDS-PAGE. Proteins were transferred to PVDF membrane (Amersham, 10600058). Immunoblotting was performed using anti-GFP at a concentration of 1:5000 (abcam, ab290), followed by secondary anti-rabbit-HRP at a concentration of 1:10,000 (abcam, ab20578).

VIGS experiments

For VIGS of *NbATG5* (*Nbe.v1.1.chr12g36840.1*), a 288-bp portion of the coding region was amplified using PCR and the amplified fragment was cloned between *Stu* I and *Mlu* I sites of the CMV-A1 vector³⁸. Plasmids containing full-length cDNA of viral RNA were transcribed in vitro and leaves of 3-week-old *Nb* plants were dusted with carborundum and rub-inoculated with the transcripts, as described previously⁵⁴. Successful infection of the virus in the upper leaves of *Nb* plants, without deletion of the inserted sequences, was confirmed via RT-PCR of the viral RNA. The primer sequences used for PCR amplification are listed in Supplementary Data 7. Primary inoculated leaves were used for secondary inoculation of *Nb* plants. Primary inoculated leaves were ground in 100 mM phosphate buffer (pH 7.0) and 10 μL of the adequate was dropped on the three expanded leaves of a new 3-week-old *Nb* and rub-inoculated. One week after inoculation (corresponding to 4 weeks of age), the infected *Nb* stem was grafted onto the bolting stem of 5-week-old *At* plants. Two weeks after grafting, the success rate was scored based on scion survival (Supplementary Data 5).

qRT-PCR

Total RNA was extracted from the plant samples using the RNeasy MinElute Cleanup Kit (Qiagen, Hilden, Germany) following the manufacturer's instructions. The RNA concentration and quality were determined using a NanoDrop One^c Spectrophotometer (Thermo Fisher Scientific, Waltham, USA). cDNA was synthesized from the RNA samples using SuperScript III First-Strand Synthesis SuperMix (Thermo Fisher Scientific) following the manufacturer's instructions. An equal concentration of cDNA from the sample comparison was used for qRT-PCR reaction with KAPA SYBR Fast qPCR Kit (Sigma-Aldrich, St. Louis, USA). To analyze the expression of genes responsive to nutrient starvation, total RNA was extracted from the graft union of *Nb* scion and *At* rootstock. For the VIGS experiments, total RNA was isolated from the stems of *Nb-grafted* plants at 3 DAG and used to produce cDNA for qRT-PCR amplification. PCR conditions were 50 °C for 2 min, 95 °C for 10 min, and 40 cycles of 95 °C for 15 s followed by 60 °C for 1 min. *NbACT1* (*Nbe.v1.1.chr19g20980.1*) was used as an internal standard. All experiments were performed using three independent biological replicates and three technical replicates. The primer sequences are shown in Supplementary Data 13.

Microscopy

For observation of resin-embedded sections, the graft regions were trimmed using a laser blade and fixed with 2% paraformaldehyde and 2% glutaraldehyde in 0.05 M cacodylate buffer (pH 7.4) at 4 °C overnight. After fixation, the samples were washed three times with 0.05 M cacodylate buffer for 30 min each and postfixed with 2% osmium tetroxide in 0.05 M cacodylate buffer at 4 °C for 3 h. The samples were dehydrated using an ethanol gradient (50%, 70%, 90%, and 100%) with the following schedule: 50% and 70% for 30 min each at 4 °C, 90% for 30 min at room temperature, and four changes of 100% for 30 min each at room temperature. Samples were dehydrated overnight in 100% ethanol at room temperature. The samples were infiltrated with propylene oxide (PO) twice for 30 min each and placed in a 70:30 (v/v) mixture of PO and resin (Quetol-651, Nissin EM Co., Tokyo, Japan) for

1 h. Then, the caps of the tubes were opened and PO was volatilized overnight. The samples were transferred to fresh 100% resin and polymerized at 60 °C for 48 h. For light microscopy, the polymerized resin blocks were sectioned at 8 µm with a microtome and mounted on slide glasses. For light microscopy, the sections were stained with 0.5% toluidine blue (pH 7.0), mounted on glass slides with Mount-Quick (DhythSangyo Co., Tokyo, Japan), and observed using a digital microscope (DMBA310, Shimadzu RIK A Co., Tokyo, Japan). For TEM analysis, the polymerized resin blocks were ultra-thin-sectioned at 80–120 nm with a diamond knife using an ultramicrotome (ULTRACUT UCT, Leica, Tokyo, Japan). The sections were mounted on copper grids and stained with 2% uranyl acetate and distilled water at room temperature for 15 min, followed by secondary staining with a lead stain solution (Sigma-Aldrich) at room temperature for 3 min. The grids were observed using a TEM (JEM-1400Plus, JEOL Ltd., Tokyo, Japan) at an acceleration voltage of 80 kV. Digital images were captured using a CCD camera (VELETA; Olympus Soft Imaging Solutions GmbH, Münster, Germany).

For immunoelectron microscopy, graft regions of *Nb/At* stem were fixed overnight at 4 °C in a mixture of 4% paraformaldehyde and 2% glutaraldehyde in 0.05 M phosphate-potassium buffer (pH 7.4). Fixed samples were dehydrated through a graded methanol series (25%, 50%, 75%, 90% and 100%). Samples were then infiltrated with LR White resin (London Resin). Polymerization was performed at 60 °C for 24 h. Ultra-thin sections (70 nm thick) were cut using an ultramicrotome (EM UC7, Leica) with a diamond knife (ultra, Diatome) and collected on nickel mesh grids. The grids were preincubated in blocking solution (Block Ace, KAC, 1:10). The sections were then incubated with primary antibodies, anti-GFP antibody (A11122; Invitrogen, 1:100; room temperature, 4 h) and anti-ATG8 antibody (ab77003; Abcam, 1:10, 4 °C, overnight), in blocking solution. After washing in blocking solution, grids were incubated with secondary antibody conjugated to 12 nm colloidal gold particles (Jackson Immuno Research Laboratories, 1:20) for 30 min at room temperature. After additional washes in blocking solution and a final wash in distilled water, the grids were post-stained with 4% uranyl acetate solution for 10 min and lead citrate solution for 1.5 min. The grids were examined and photographed using a transmission electron microscope (JEM-1400 Flash, JEOL) with a CMOS digital camera at an acceleration voltage of 80 kV.

For SEM analysis, graft regions of *Nb/At* and *At/At* hypocotyl were dissected with scissors. Samples were embedded with low-melting-point agarose to protect the graft junction. Samples were pre-fixed in a mixture of 4% (w/v) paraformaldehyde and 2% (v/v) glutaraldehyde in 0.05 M sodium cacodylate buffer (pH 7.4) at 4 °C overnight, then post-fixed with 1% (v/v) osmium tetroxide in same buffer for 3 h at room temperature. Then the samples were dehydrated in a graded methanol series (25%, 50%, 70%, 90% and 100%), replaced with propylene oxide, infiltrated with increasing concentrations of Epon812 resin (TAAB) and finally embedded in 100% resin. Semi-thin sections (500 nm thick) were cut using an ultramicrotome (EM UC7, Leica) with a diamond knife (histo, Diatome) and mounted on glass slides. After staining with 0.4% (w/v) uranyl acetate solution for 10 min and lead citrate solution for 2 min, the sections were coated with osmium coater (HPC-1SW, Vacuum Device) for 3 s. Images were obtained using a field emission scanning electron microscope (FE-SEM, Regulus 8240, Hitachi) with an yttrium aluminum garnet (YAG) backscattered electron detector at an acceleration voltage of 5 kV.

For localization of GFP-ATG8 in *Nb/At* stem graft, graft sections were treated with ClearSee™ (Fujifilm, Tokyo, Japan) and mounted on glass slides. The slides were examined under a confocal laser-scanning microscope (FV3000; Olympus, Tokyo, Japan). A 488-nm excitation laser and a collection emission spectrum with a machine setting ranged 487–530 nm was used for GFP fluorescence detection. More than three independent samples were observed for all sample fractions. Graft regions of the *Nb/Nb* and the *Nb/At* hypocotyl grafts were

observed under the CLSM (FV3000; Fig. 3a–i, Fig. 4a–h). A 488-nm excitation laser and a collection emission spectrum with a machine setting ranged 487–530 nm was used for GFP fluorescence detection. A 561 nm excitation laser and collection emission spectrum 574–602 nm were used for RFP fluorescence detection. For the *Nb/At* and the *Nb/Nb* grafts, maximum intensity projection (MIP) images were acquired from z-stack images composed of 25 steps (the step intervals: the *Nb/At*; 2.5 µm, the *Nb/Nb*; 5.0 µm) using cellSens FV software (Olympus, Tokyo, Japan). The MIP images of the *Nb/At* and the *Nb/Nb* grafts were adjusted to a brightness level that was increased by 20%. Graft regions of the *Nb/Nb* and the *At/At* hypocotyl grafts were observed under the CLSM (LSM880; Carl Zeiss, Oberkochen, Germany; Fig. 4j–n, Fig. 5a–p). A 488-nm excitation laser and a collection emission spectrum of 493–598 nm was used for GFP fluorescence detection. MIP images were acquired from z-stack images composed of 35 steps (the step intervals: the *At/At*, 3.0 µm) among the observed z-stack images using ZEN lite software (Carl Zeiss, Oberkochen, Germany). Fluorescent dot-like signals observed in the scion and stock areas of the MIP images were counted as autophagosomes. The number of autophagosomes is normalized by each area (per 0.1 mm²). The image data is available at BioImage Archive (<https://www.ebi.ac.uk/biostudies/bioimages/studies/S-BIAD1557>).

Statistical analysis

All statistical analyses were performed using scripts and applications built using Python version 3.7.4 and its library modules, NumPy (1.17.2), Pandas (0.25.1), SciPy (1.3.1), and StatsModels (0.10.2).

Reporting summary

Further information on research design is available in the Nature Portfolio Reporting Summary linked to this article.

Data availability

RNA-Seq data are available from the DNA Data Bank of Japan (DDBJ; <http://www.ddbj.nig.ac.jp/>) under the accession number DRA009936. Source data for qRT-PCR and Western blots are provided with this paper. Source data are provided with this paper.

References

- Davies, Jr. F. T., Geneve, R. L. & Wilson, S. B. *Hartmann & Kester's Plant Propagation: Principles and Practices*, 9th edn. 490–542 (Pearson, NY, 2018).
- Gaut, B. S., Miller, A. J. & Seymour, D. K. Living with two genomes: grafting and its implications for plant genome-to-genome interactions, phenotypic variation, and evolution. *Annu. Rev. Genet.* **53**, 51–5.21 (2019).
- Thomas, H. R. & Frank, M. H. Connecting the pieces: uncovering the molecular basis for long-distance communication through plant grafting. *N. Phytol.* **223**, 582–589 (2019).
- Notaguchi, M. et al. Cell-cell adhesion in plant grafting is facilitated by β-1,4-glucanases. *Science* **369**, 698–702 (2020).
- Kurotani, K. et al. Host-parasite tissue adhesion by a secreted type of β-1,4-glucanase in the parasitic plant *Phtheirospermum japonicum*. *Commun. Biol.* **3**, 407 (2020).
- Kurotani, K. et al. *Discovery Of The Interfamily Grafting Capacity Of Petunia, A Floricultural Species*. *Hort. Res.* **9**, uhab056 (2022).
- Reeves, G. et al. Monocotyledonous plants graft at the embryonic root-shoot interface. *Nature* (2021).
- Cookson, M. J. et al. Heterografting with nonself rootstocks induces genes involved in stress responses at the graft interface when compared with autografted controls. *J. Exp. Bot.* **65**, 2473–2481 (2014).
- Assunção, M., Santos, C., Brazão, J., Eiras-Dias, J. E. & Fevereiro, P. Understanding the molecular mechanisms underlying graft success in grapevine. *BMC Plant Biol.* **19**, 396 (2019).

10. Chen, Z. et al. Transcriptome changes between compatible and incompatible graft combination of Litchi chinensis by digital gene expression profile. *Sci. Rep.* **7**, 3954 (2017).
11. Xie, L., Dong, C. & Shang, Q. Gene co-expression network analysis reveals pathways associated with graft healing by asymmetric profiling in tomato. *BMC Plant Biol.* **19**, 373 (2019).
12. Wang, H., Zhou, P., Zhu, W. & Wang, F. De novo comparative transcriptome analysis of genes differentially expressed in the scion of homografted and heterografted tomato seedlings. *Sci. Rep.* **9**, 20240 (2019).
13. Bantis, F. et al. Comparative transcriptome analysis in homo- and hetero-grafted cucurbit seedlings. *Front. Plant Sci.* **12**, 691069 (2021).
14. Melnyk, C. W., Schuster, C., Leyser, O. & Meyerowitz, E. M. A developmental framework for graft formation and vascular reconnection in *Arabidopsis thaliana*. *Curr. Biol.* **25**, 1306–1318 (2015).
15. Matsuoka, K. et al. Differential cellular control by cotyledon-derived phytohormones involved in graft reunion of *Arabidopsis* hypocotyls. *Plant Cell Physiol.* **57**, 2620–2631 (2016).
16. Melnyk, C. W. et al. Transcriptome dynamics at *Arabidopsis* graft junctions reveal an inter tissue recognition mechanism that activates vascular regeneration. *Proc. Natl Acad. Sci. USA.* **115**, E2447–E2456 (2018).
17. Moore, R. & Walker, D. B. Studies of vegetative compatibility-incompatibility in higher plants. I. a structural study of a compatible autograft in *Sedum telephoides* (Crassulaceae). *Amj. Bot.* **68**, 820–830 (1981).
18. Jeffree, C. E. & Yeoman, M. M. Development of intercellular connections between opposing cells in a graft union. *N. Phytol.* **93**, 491–509 (1983).
19. Sala, K., Karcz, J., Rypień, A. & Kurczyńska, E. U. Unmethyl-esterified homogalacturonan and extensins seal *Arabidopsis* graft union. *BMC Plant Biol.* **19**, 151 (2019).
20. Kollmann, R., Yang, S. & Glockmann, C. Studies on graft unions II. Continuous and half plasmodesmata in different regions of the graft interface. *Protoplasma* **126**, 19–29 (1985).
21. Chambaud, C., Cookson, S. J., Ollat, N., Bayer, E. & Brocard, L. A correlative light electron microscopy approach reveals plasmodesmata ultrastructure at the graft interface. *Plant Physiol.* **188**, 44–45 (2021).
22. Kurotani, K. & Notaguchi, M. Cell-to-cell connection in plant grafting—molecular insights into symplasmic reconstruction. *Plant Cell Physiol.* **62**, 1362–1371 (2021).
23. Farré, J. C. & Subramani, S. Mechanistic insights into selective autophagy pathways: lessons from yeast. *Nat. Rev. Mol. Cell Biol.* **17**, 537–552 (2016).
24. Li, F. & Vierstra, R. D. Autophagy: a multifaceted intracellular system for bulk and selective recycling. *Trends Plant Sci.* **17**, 526–537 (2012).
25. Liu, Y. & Bassham, D. C. Autophagy: pathways for self-eating in plant cells. *Annu. Rev. Plant Biol.* **63**, 215–237 (2012).
26. Bassham, D. C. et al. Autophagy in development and stress responses of plants. *Autophagy* **2**, 2–11 (2006).
27. van Doorn, W. G. & Papini, A. Ultrastructure of autophagy in plant cells: a review. *Autophagy* **9**, 1922e1936 (2013).
28. Yoshimoto, K. Beginning to understand autophagy, an intracellular self-degradation system in plants. *Plant Cell Physiol.* **53**, 1355–1365 (2012).
29. Soto-Burgos, J., Zhuang, X., Jiang, L. & Bassham, D. C. Dynamics of autophagosome formation. *Plant Physiol.* **176**, 219–229 (2018).
30. Zhuang, X. et al. ATG9 regulates autophagosome progression from the endoplasmic reticulum in *Arabidopsis*. *Proc. Natl Acad. Sci. USA.* **114**, E426–E435 (2017).
31. Gómez-Sánchez, R. et al. *Atg2* establishes *Atg2*-dependent contact sites between the endoplasmic reticulum and phagophores. *J. Cell Biol.* **217**, 2743–2763 (2018).
32. Doelling, J. H., Walker, J. M., Friedman, E. M., Thompson, A. R. & Vierstra, R. D. The APG8/12-activating enzyme APG7 is required for proper nutrient recycling and senescence. *Arabidopsis thaliana. J. Biol. Chem.* **277**, 33105–33114 (2002).
33. Thompson, A. R., Doelling, J. H., Suttangkakul, A. & Vierstra, R. D. Autophagic nutrient recycling in *Arabidopsis* directed by the ATG8 and ATG12 conjugation pathways. *Plant Physiol.* **138**, 2097–2110 (2005).
34. Huang, C. et al. *Nicotiana benthamiana* XYLEM CYSTEINE PROTEASE genes facilitate tracheary element formation in interfamily grafting. *Horticulture Res.* **10**, uhad072 (2023).
35. Yoshimoto, K. et al. Processing of ATG8s, ubiquitin-like proteins, and their deconjugation by ATG4s are essential for plant autophagy. *Plant Cell* **16**, 2967–2983 (2004).
36. Izumi, M., Ishida, H., Nakamura, S. & Hidema, J. Entire photo-damaged chloroplasts are transported to the central vacuole by autophagy. *Plant Cell* **29**, 377–394 (2017).
37. Tsutsui, H. et al. Micrografting device for testing environmental conditions for grafting and systemic signaling in *Arabidopsis*. *Plant J.* **103**, 918–929 (2020).
38. Otagaki, S., Kawai, M., Masuta, C. & Kanazawa, A. Size and positional effects of promoter RNA segments on virus-induced RNA-directed DNA methylation and transcriptional gene silencing. *Epigenetics* **6**, 681–691 (2011).
39. Hammond, J. et al. Changes in gene expression in *Arabidopsis* shoots during phosphate starvation and the potential for developing smart plants. *Plant Physiol.* **132**, 578–596 (2003).
40. Krapp, A. et al. *Arabidopsis* roots and shoots show distinct temporal adaptation patterns toward nitrogen starvation. *Plant Physiol.* **157**, 1255–1282 (2011).
41. Kiba, T. et al. Repression of Nitrogen-Starvation Responses by Members of the *Arabidopsis* GARP-Type Transcription Factor NIGT1/HRS1 Subfamily. *Plant Cell* **30**, 925–945 (2018).
42. Bostock, R. M. & Stermer, B. A. Perspectives on wound healing in resistance to pathogens. *Annu. Rev. Phytopathol.* **27**, 343–371 (1989).
43. Rodriguez, E. et al. Autophagy mediates temporary reprogramming and dedifferentiation in plant somatic cells. *EMBO J.* **39**, e103315 (2020).
44. Galili, G., Avin-Wittenberg, T., Angelovici, R. & Fernie, A. R. The role of photosynthesis and amino acid metabolism in the energy status during seed development. *Front. Plant Sci.* **5**, 447 (2014).
45. Asahina, M. et al. Spatially selective hormonal control of RAP2.6 L and ANACO71 transcription factors involved in tissue reunion in *Arabidopsis*. *Proc. Natl Acad. Sci. USA.* **108**, 16128–16132 (2011).
46. Ikeuchi, M., Sugimoto, K. & Iwase, A. Plant callus: Mechanisms of induction and repression. *Plant Cell* **25**, 3159–3173 (2013).
47. Ikeuchi, M. et al. Wound-inducible WUSCHEL-RELATED HOMEBOX 13 is required for callus growth and organ reconnection. *Plant Physiol.* **188**, 425–441 (2022).
48. Tanaka, H. et al. Auxin-Induced WUSCHEL-RELATED HOMEBOX13 Mediates asymmetric activity of callus formation upon cutting. *Plant Cell Physiol.* **64**, 305–316 (2023).
49. Thomas, H., Van den Broeck, L., Spurney, R., Sozzani, R. & Frank, M. Gene regulatory networks for compatible versus incompatible grafts identify a role for *SlWOX4* during junction formation. *Plant Cell* **34**, 535–556 (2022).
50. Fujiwara, T., Hirai, M. Y., Chino, M., Komeda, Y. & Naito, S. Effects of sulfur nutrition on expression of the soybean seed storage protein genes in transgenic petunia. *Plant Physiol.* **99**, 263–268 (1992).
51. Okayasu, K., Aoki, K., Kurotani, K. & Notaguchi, M. Tissue adhesion between distant plant species in parasitism and grafting. *Commun. Integr. Biol.* **14**, 21–23 (2021).
52. Tsutsui, H., Kawakatsu, Y. & Notaguchi, M. Micrografting in *Arabidopsis* using a silicon chip. *Bio Protoc.* **11**, e4053 (2021).

53. Sugita, R. et al. Visualization of uptake of mineral elements and the dynamics of photosynthates in *arabidopsis* by a newly developed real-time radioisotope imaging system (RRIS). *Plant Cell Physiol.* **57**, 743–753 (2016).
54. Otagaki, S. et al. Rapid induction of transcriptional and post-transcriptional gene silencing using a novel Cucumber mosaic virus vector. *Plant Biotechnol.* **23**, 259–265 (2006).

Acknowledgements

We thank M. Hattori, M. Matsumoto, I. Yoshikawa, A. Yagi and M. Taniguchi for technical assistance. We are grateful to C. Masuta (Hokkaido University, Japan) for providing CMV vectors and S. Otagaki (Nagoya University, Japan) for advising VIGS experiments. We thank R. Sato and T. Okada (RIKEN IMS) for offering the field emission scanning electron microscope. This work was supported by grants from the Japan Society for the Promotion of Science Grants-in-Aid for Scientific Research (18KT0040, 19H05361, 20H03273, 21H00368, 21H05657 and 25H01341 to MN, 22K06181 to KK, 19H05713 to KY, and 22H04926 and 24H02142 to KiT), the Japan Science and Technology Agency (JPMJTR194G to MN), New Energy and Industrial Technology Development Organization (JPNP20004 to MN) and the Canon Foundation (R17-0070 to MN).

Author contributions

K.K., K.Y. and M.N. conceived of the research and designed experiments. Y.K., Ke.O., D.S., R.T. and Ko.O. performed grafting experiments, R.S. and K.T. performed radio isotope experiments, R.T. performed VIGS experiments, K.K. performed expression analysis and K.K., D.S., Y.U., M.M., Ke.O., Y.G., M.S. and Ki.T. performed microscopy analysis. K.K. and M.N. wrote the paper.

Competing interests

The authors declare no competing interests.

Additional information

Supplementary information The online version contains supplementary material available at <https://doi.org/10.1038/s41467-025-58519-6>.

Correspondence and requests for materials should be addressed to Kohki Yoshimoto or Michitaka Notaguchi.

Peer review information *Nature Communications* thanks Lysiane Brocard and the other, anonymous, reviewer(s) for their contribution to the peer review of this work. A peer review file is available.

Reprints and permissions information is available at <http://www.nature.com/reprints>

Publisher's note Springer Nature remains neutral with regard to jurisdictional claims in published maps and institutional affiliations.

Open Access This article is licensed under a Creative Commons Attribution-NonCommercial-NoDerivatives 4.0 International License, which permits any non-commercial use, sharing, distribution and reproduction in any medium or format, as long as you give appropriate credit to the original author(s) and the source, provide a link to the Creative Commons licence, and indicate if you modified the licensed material. You do not have permission under this licence to share adapted material derived from this article or parts of it. The images or other third party material in this article are included in the article's Creative Commons licence, unless indicated otherwise in a credit line to the material. If material is not included in the article's Creative Commons licence and your intended use is not permitted by statutory regulation or exceeds the permitted use, you will need to obtain permission directly from the copyright holder. To view a copy of this licence, visit <http://creativecommons.org/licenses/by-nc-nd/4.0/>.

© The Author(s) 2025